Crystal structure and electronic property modification of Ca_2RuO_4 thin films via fluorine doping

Shota Fukuma,[1] Akira Chikamatsu [1,2,*] Tsukasa Katayama [3,4] Takahiro Maruyama,[1] Keiichi Yanagisawa [5]
Koji Kimoto,[5] Miho Kitamura,[6] Koji Horiba,[7] Hiroshi Kumigashira,[8] Yasushi Hirose [1] and Tetsuya Hasegawa[1]

[1]*Department of Chemistry, The University of Tokyo, 7-3-1 Hongo, Bunkyo-ku, Tokyo 113-0033, Japan*
[2]*Department of Chemistry, Faculty of Science, Ochanomizu University, 2-1-1 Otsuka, Bunkyo-ku, Tokyo 112-8610, Japan*
[3]*Research Institute for Electronic Science, Hokkaido University, N20W10, Kita, Sapporo 001-0020, Japan*
[4]*Japan Science and Technology Agency (JST) PRESTO, 4-1-8 Honcho, Kawaguchi, Saitama 332-0012, Japan*
[5]*National Institute for Materials Science, 1-1 Namiki, Tsukuba, Ibaraki 305-0044, Japan*
[6]*Institute of Materials Structure Science, High Energy Accelerator Research Organization (KEK), 1-1 Oho, Tsukuba, Ibaraki 305-0801, Japan*
[7]*National Institutes for Quantum and Radiological Science and Technology, 1-1-1 Kouto, Sayo-cho, Sayo-gun, Hyogo 679-5148, Japan*
[8]*Institute of Multidisciplinary Research for Advanced Materials, Tohoku University, 2-1-1 Katahira, Aoba-ku, Sendai 980-8577, Japan*

Layered ruthenium oxyfluorides have various crystal structures and Ru oxidation states and exhibit unique physical properties. While various layered ruthenates have reportedly been topochemically fluorinated with Sr as A sites, investigation of the fluorination of layered ruthenates containing smaller Ca ions is lacking. In this paper, we fabricated phase-pure and single-crystalline thin films of $Ca_2RuO_{2.5}F_2$ on $LaSrAlO_4$ (001) substrates via topochemical fluorination of the Ca_2RuO_4 precursor using polyvinylidene fluoride. The obtained fluorinated thin films had a chemical composition of $Ca_2RuO_{2.5}F_2$ with the Ru^{3+} state, as determined by energy-dispersive x-ray spectroscopy and x-ray photoemission spectroscopy, whereas the film prepared via $Sr_2Ru^{4+}O_4$ fluorination had a composition of $Sr_2Ru^{4+}O_3F_2$. Scanning transmission electron microscopy revealed that $Ca_2RuO_{2.5}F_2$ has only 1 F^- site in CaO rock-salt blocks, whereas $Sr_2RuO_3F_2$ has two inequivalent F^- sites in the SrO layers. The $Ca_2RuO_{2.5}F_2$ film was insulating, with a resistivity (ρ) of $8.6 \times 10^{-2} \Omega$ cm at 300 K. Moreover, the temperature behavior of ρ was well described by the two-dimensional variable range hopping model. These results demonstrate that local distortion is an important factor that governs the topochemical fluorination of ruthenates and affects the crystal and electronic structures of the reactants.

I. INTRODUCTION

Topochemical fluorination has been established as a chemical technique that can modify the electronic properties of transition metal oxides. For example, ferromagnetic $SrMnO_{2-x}F_{1+x}$ is obtained through the fluorination of antiferromagnetic $SrMnO_{2.5}$ [1,2], and Mott-insulating $NdNiO_{3-x}F_x$ is synthesized by the topochemical fluorination of metallic $NdNiO_3$ [3]. Topochemical fluorination includes two types of reactions: insertion of F^- into interstitial or interlayer sites and substitution of F^- for O^{2-}. The former is accompanied by the oxidation of a transition metal cation [4–9], whereas the latter proceeds through the reduction of a transition metal cation [3,10–17].

In the topochemical fluorination of layered perovskites $A_{n+1}B_nO_{3n+1}$ (A = alkali metal, alkaline earth, or rare earth; B = transition metal) consisting of BO_6 octahedral and AO rock-salt layers, insertion and substitution could occur simultaneously; one or two F^- ions are inserted into each AO block, and the O^{2-} ions in the BO_6 block are partially substituted with F^- [7,17–20]. Thus, the B cation can have various oxidation states depending on the fluorine content [7]. The fluorination of layered ruthenates has been extensively studied

in terms of the modification of their magnetic properties as a function of the Ru oxidation state, ranging from 4+ to 6+ [6,7,19,21]. For example, antiferromagnetic $Sr_3Ru_2^{5+}O_7F_2$ and $Sr_3Mn^{4+}Ru^{6+}O_7F_2$ and paramagnetic $Sr_3Ti^{4+}Ru^{6+}O_7F_2$ are obtained by the topochemical fluorination of paramagnetic $Sr_3Ru_2^{4+}O_7$, spin-glass $Sr_3Mn^{4+}Ru^{4+}O_7$, and antiferromagnetic $Sr_3Ti^{4+}Ru^{4+}O_7$, respectively, wherein only the insertion of F^- SrO rock-salt layers occurs [6,7]. Moreover, antiferromagnetic $Sr_3Fe^{3+}Ru^{5.5+}O_{5.5}F_{3.5}$ and Mott-insulating $Sr_2Ru^{4+}O_3F_2$ are synthesized by the fluorination of spin-glass $Sr_3Fe^{3+}Ru^{5+}O_7$ and superconductor $Sr_2Ru^{4+}O_4$, wherein both the insertion of F^- in SrO and F^- substitution in RuO_6 occur simultaneously [7,19,21]. However, investigation of topochemically fluorinating layered ruthenates at different A cations is lacking.

In this paper, we focused on a layered perovskite Ca_2RuO_4 epitaxial thin film as a precursor for topochemical fluorination. Ca_2RuO_4 has a crystal structure wherein isovalent Ca ions were substituted with Sr ions in superconductor Sr_2RuO_4 but exhibits insulating behavior at <300 K due to large RuO_6 octahedral distortion [22,23]. Indeed, the Ru–O–Ru bond angle of Ca_2RuO_4 (151$°$ at 11 K) is considerably smaller than that of Sr_2RuO_4 (180$°$), and Ca_2RuO_4 undergoes an insulator to (near-) metal transition at 357 K, driven by a structural phase transition to a less distorted phase [22,24]. Thus, comparative structural analysis between oxyfluorides

*Corresponding author: chikamatsu.akira@ocha.ac.jp

prepared from Sr_2RuO_4 and Ca_2RuO_4 would provide insights into the influence of local distortion during the topochemical fluorination of layered perovskites.

Herein, we report the incorporation of fluorine into Ca_2RuO_4 epitaxial thin films by topochemical fluorination using polyvinylidene fluoride (PVDF). The obtained fluorinated thin films had a chemical composition of $Ca_2RuO_{2.5}F_2$ and a Ru^{3+} state, as determined by energy-dispersive x-ray spectroscopy (EDS) and x-ray photoemission spectroscopy (XPS). Scanning transmission electron microscopy (STEM) revealed that the intercalation of anions occurs in the CaO layer. The in-plane electrical resistivity of the $Ca_2RuO_{2.5}F_2$ film was well described by a two-dimensional (2D) variable range hopping model.

II. EXPERIMENTAL SECTION

Layered perovskite Ca_2RuO_4 precursor films were grown through solid-phase epitaxy. Precursor $CaRuO_x$ films were deposited on $LaSrAlO_4$ (001) (LSAO, CrysTech Co.) substrates using the pulsed laser deposition (PLD) technique. A polycrystalline $CaRuO_3$ ceramic pellet was used as a target for PLD and was ablated by a KrF excimer laser (wavelength $\lambda = 248$ nm). During the deposition, the substrate temperature and pressure inside the chamber were set at 20–25 °C and 1×10^{-8} Torr, respectively. The obtained amorphous films with thicknesses of $\sim$60 nm were crystallized to single-crystalline Ca_2RuO_4 by annealing at 1200 °C for 2 h in air. A polycrystalline pellet of $CaRuO_3$ was heated with the amorphous films to suppress the loss of volatile ruthenium in the films during annealing. The crystallized Ca_2RuO_4 films were subsequently fluorinated by heating with PVDF (Fluorochem Ltd.) under Ar gas flow at 220 °C for 12 h. Following the methodology previously developed by our group [12], the films were covered with Al foil during fluorination to avoid the adhesion of the charcoallike residue produced during the decomposition of PVDF.

The crystal structures of the films were characterized by x-ray diffraction (XRD) analysis conducted using Cu-$K\alpha$ radiation (D8 DISCOVER, Bruker). A diffractometer in parallel beam geometry was equipped with one-dimensional and 2D detectors so that both in-plane and out-of-plane lattice constants can be calculated from the obtained diffraction patterns. The chemical compositions were determined through EDS (JED-2300, JEOL) in conjunction with a scanning electron microscope (JSM-7100F, JEOL). Ru $3p$ and Ca $2p$ XPS spectra were measured at 300 K using a VG-SCIENTA SES-2002 electron energy analyzer with an energy resolution of 300 meV at a photon energy of 1200 eV. The Fermi level of the samples was set as that of an *in situ* evaporated gold foil that was in electrical contact with the sample. STEM images were acquired using an aberration-corrected microscope (Titan cubed, FEI) operating at an acceleration voltage of 300 kV. The convergence semiangle of the incident probe was 18 mrad, while the detector collection semiangles were 45.8–200 mrad for annular dark-field (ADF) and 9–18 mrad for annular bright-field (ABF) imaging. The STEM images were filtered using a Fourier filter for noise reduction. A thin specimen for STEM observation was prepared using a focused ion beam (FIB) instrument (FB-2000, Hitachi High-
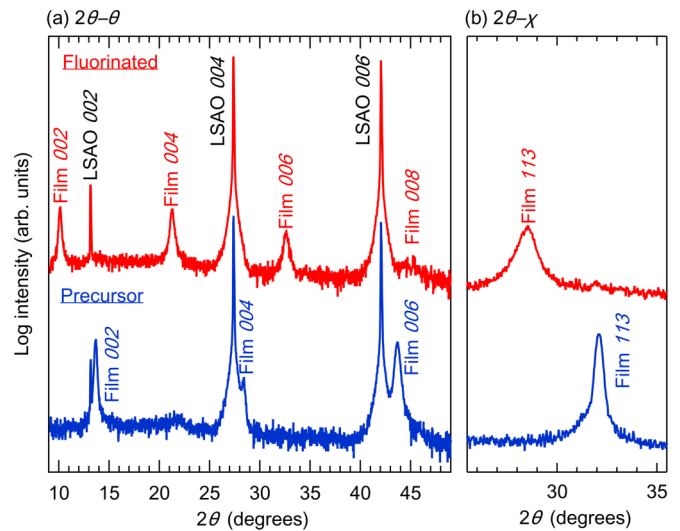

FIG. 1. (a) 2θ-θ and (b) 2θ-χ x-ray diffraction (XRD) patterns of the Ca_2RuO_4 precursor and the film fluorinated at 220 °C for 12 h on LSAO substrates. The 2θ-χ patterns of the precursor and fluorinated film were integrated in the ranges of $\chi = 45−46.5°$ and $48−52°$, respectively.

Tech). In-plane electrical resistivities (ρ) were measured by the four-terminal method with gold electrodes using a physical property measurement system (Quantum Design Co.), in which the maximum measurement range for ρ was 100 Ω cm at this thickness. The crystal structures were visualized using the VESTA program [25].

III. RESULTS AND DISCUSSION

Figure 1 shows the 2θ-θ and 2θ-χ XRD patterns of the Ca_2RuO_4 precursor film and the film after fluorination with PVDF at 220 °C, where 2θ describes the diffraction angle given by Bragg's law and χ denotes the rotation of the scattering vector from out of plane ($\chi = 90°$) toward in plane ($\chi = 0°$). The 2θ-θ spectrum of the Ca_2RuO_4 precursor exhibited diffractions of 002, 004, and 006 planes, indicating the presence of the single-layered perovskite structure. The 2θ-χ XRD patterns in Fig. 1(b) were obtained from the 2D 2θ-χ images (Fig. S1 in the Supplemental Material [26]). As seen in Fig. S1, 113 diffraction spots of the precursor film were observed in the 2θ-χ image near the LSAO 113 diffraction spot, indicating that the precursor film has the same in-plane orientation as the LSAO substrate. These results suggest the epitaxial growth of a c-axis-oriented Ca_2RuO_4 film. The lattice constants of the precursor film were calculated to be $a = 5.41$ Å and $c = 12.15$ Å, which were larger and smaller, respectively, than those of the coherently grown thin film of Ca_2RuO_4 on an LSAO substrate ($a = 5.31$ Å, $c = 12.37$ Å) [27], indicating that our film was strain relaxed. The 2θ-θ spectrum of the fluorinated film also showed 002, 004, 006, and 008 diffractions without those for any impurity phases, such as CaF_2 and CaO, but the c-axis length was extended to 16.25 Å. In contrast, the a-axis length was unchanged (5.41 Å) even after fluorination. Such anisotropic lattice expansion with fluorination has been reported in other layered
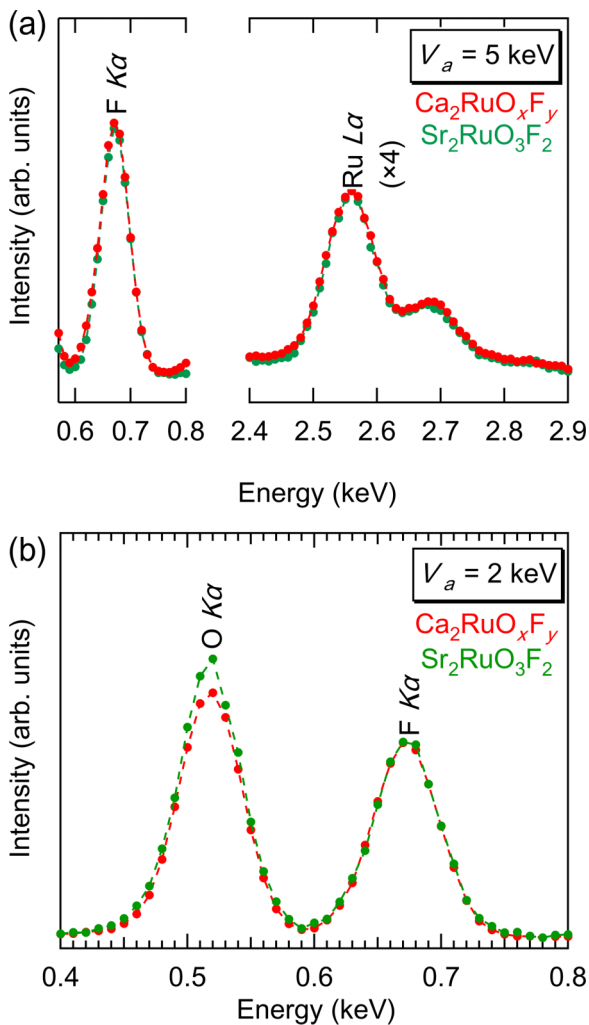
FIG. 2. Energy-dispersive x-ray spectroscopy (EDS) spectra of the fluorinated film ($Ca_2RuO_xF_y$) compared with those of the $Sr_2RuO_3F_2$ thin film at (a) 5 keV and (b) 2 keV. Note that the Ru peaks shown in (a) have been multiplied by 4.

perovskites such as Sr_2RuO_4 [19], Sr_2IrO_4 [20], and Sr_2TiO_4 [28].

Figure 2(a) shows a 5 keV EDS spectrum of the fluorinated film ($Ca_2RuO_xF_y$). The figure also includes the spectrum of a $Sr_2RuO_3F_2$ thin film, whose chemical composition was determined by hard XPS and elastic recoil detection analysis, for comparison [19]. Both films showed the same Ru $L\alpha$: F $K\alpha$ peak area ratio, indicating that the F content of the $Ca_2RuO_xF_y$ film y was 2. Figure 2(b) compares the 2 keV EDS spectra of the $Ca_2RuO_xF_y$ and $Sr_2RuO_3F_2$ thin films, normalized by the F $K\alpha$ peak height. This acceleration voltage (2 keV) was sufficiently low to suppress the contribution from the substrate, as confirmed by a Monte Carlo simulation of the electron trajectory in solids [29]. As shown in Fig. 2(b), the S_O/S_F ratio of the $Ca_2RuO_xF_y$ film (1.21) was smaller than that of the $Sr_2RuO_3F_2$ film (1.34), where S_O and S_F are the peak areas corresponding to O $K\alpha$ and F $K\alpha$, respectively. Based on the EDS results, the x value for the $Ca_2RuO_xF_y$ film was estimated to be 2.7 ± 0.3.
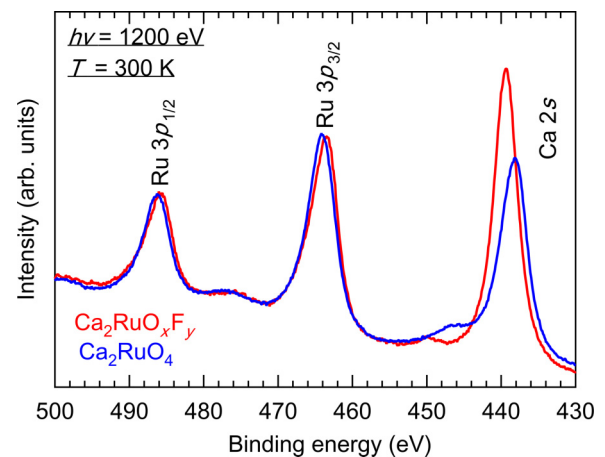

FIG. 3. Ru $3p$ and Ca $2s$ x-ray photoemission spectroscopy (XPS) spectra of the Ca_2RuO_4 precursor and the fluorinated films. The spectra were normalized by the peak height corresponding to Ru $3p_{3/2}$.

To investigate the valence of Ru, core-level XPS spectra of Ru $3p$ and Ca $2s$ for the Ca_2RuO_4 and fluorinated films were measured, as shown in Fig. 3. In the spectrum of the Ca_2RuO_4 film, the Ru spin-orbit split doublet —$3p_{1/2}$ and $3p_{3/2}$— and the Ca $2s$ peak were clearly observed at binding energies (E_b) of 486.3, 464.2, and 438.2 eV, respectively. Upon fluorination, the Ru $3p$ peaks shifted to a 0.5 eV lower binding energy, suggesting that the valence of Ru in the fluorinated film is 3+, which is consistent with the chemical composition determined by EDS. This XPS result contrasts with the fluorination of $Sr_2Ru^{4+}O_4$ to $Sr_2Ru^{4+}O_3F_2$, in which no peak shift of Ru $3p$ was observed [21]. It is speculated that the larger lattice distortion in Ca_2RuO_4, which originates from the smaller ionic radius of Ca, leads to the easier release of oxygen from the RuO_6 octahedra. Considering the EDS (Fig. 2) and XPS (Fig. 3) results, we tentatively determined the chemical composition of the fluorinated thin film as $Ca_2RuO_{2.5}F_2$. In contrast to the Ru $3p$ peaks, the Ca $2s$ peak shifted to a 1.2 eV higher binding energy upon fluorination, which suggests a change in the bonding environment around Ca [21,30,31].

To observe the microscopic structure of the films directly, high-resolution TEM measurements were performed. Figure 4 shows cross-sectional ADF-STEM images of the Ca_2RuO_4 precursor and $Ca_2RuO_{2.5}F_2$ films taken along [110]. From the figure, Ru and Ca atomic columns and the expansion of the interval between layers upon fluorination were clearly observed. The c-axis lengths of the Ca_2RuO_4 precursor and the $Ca_2RuO_{2.5}F_2$ films were evaluated to be 12.2 and 15.9 Å, respectively, almost consistent with those obtained from the XRD measurements. Figure S2(a) in the Supplemental Material [26] shows a magnified cross-sectional ADF-STEM image of the $Ca_2RuO_{2.5}F_2$ film, taken along [110], in which two Ca columns between adjacent Ru columns are clearly resolved.

Cross-sectional ABF-STEM measurements, which are more sensitive to light elements, were also conducted. Figure 5(a) is an ABF-STEM image of the $Ca_2RuO_{2.5}F_2$ film, taken along [100], in which atomic columns between the Ca and Ca atomic planes are clearly resolved. Although ABF-
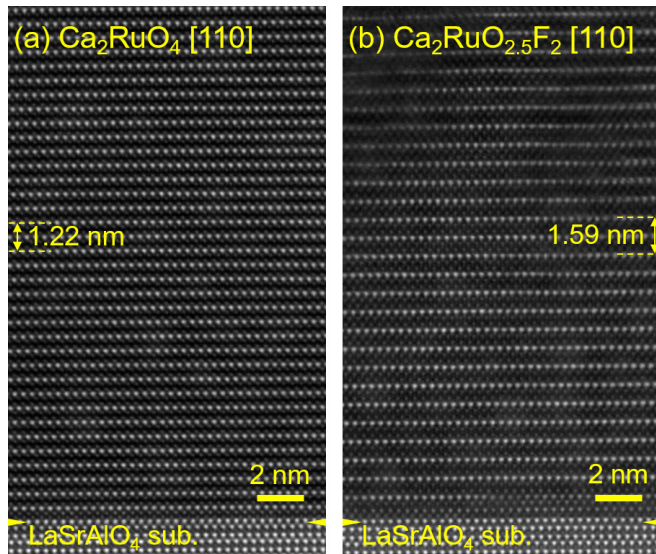
FIG. 4. Cross-sectional annular dark-field (ADF) scanning transmission electron microscopy (STEM) images of (a) the Ca_2RuO_4 precursor and (b) the $Ca_2RuO_{2.5}F_2$ films on LSAO substrates taken along [110].

STEM cannot distinguish between oxygen and fluorine, it can be assumed that the atomic column represents fluorine inserted into the CaO rock-salt blocks upon fluorination. Anion columns, possibly corresponding to the oxygen atoms forming the RuO_6 octahedra, were also visible between the Ru columns.

According to density functional theory calculations [21], $Sr_2RuO_3F_2$ has two inequivalent F^- sites and, as a result, alternating long and short Ca–Ca spacings along the c axis, as illustrated in Fig. S3(b) in the Supplemental Material [26]. However, as observed from the cation column intensity profile
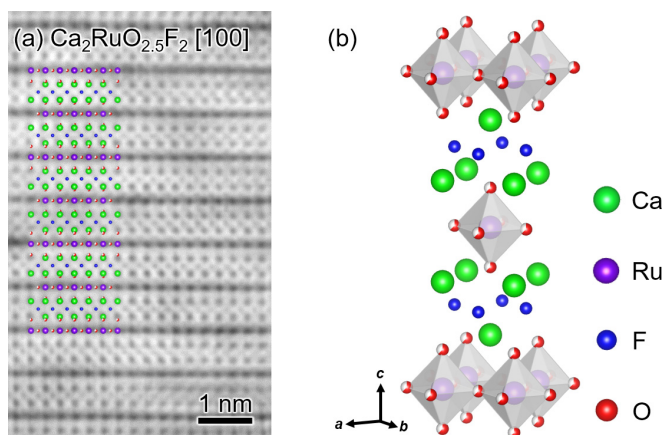

FIG. 5. (a) Cross-sectional annular bright-field (ABF) scanning transmission electron microscopy (STEM) image of the $Ca_2RuO_{2.5}F_2$ film taken along [100], together with the estimated schematic crystal structure. (b) Estimated schematic crystal structure of $Ca_2RuO_{2.5}F_2$. It is postulated that the Ru–O–Ru bond angle is $90°$, that the fluoride ions are intercalated only into the CaO rock-salt layer, and that the positions of the oxygen vacancies are expressed based on an average.
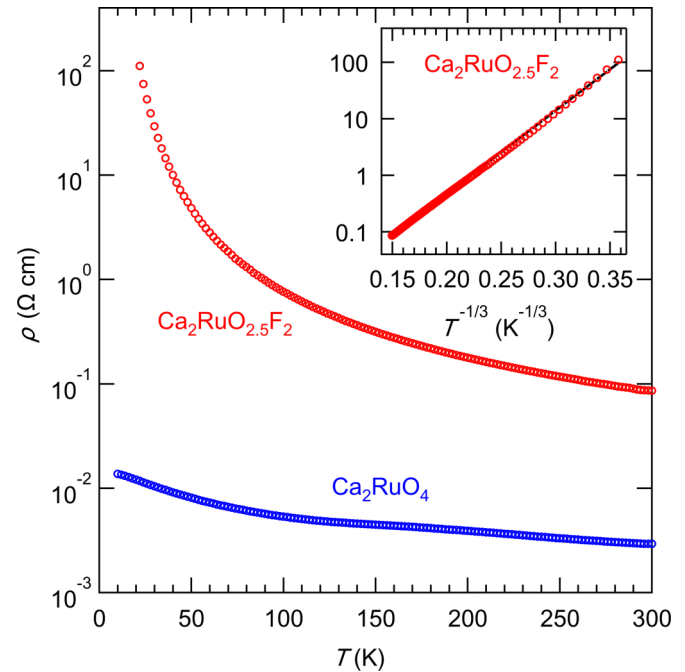

FIG. 6. Temperature dependence of the electrical resistivity for Ca_2RuO_4 precursor and $Ca_2RuO_{2.5}F_2$ films. The inset plots ρ vs $T^{-1/3}$.

perpendicular to the film plane (Fig. S2(b) in the Supplemental Material [26]), the experimentally observed Ca–Ca atomic spacing was uniform, 0.29 nm, suggesting that $Ca_2RuO_{2.5}F_2$ has only one F^- site. Based on the TEM results, we propose the crystal structure of $Ca_2RuO_{2.5}F_2$, illustrated in Fig. 5(b), where it is postulated that the Ru–O–Ru bond angle is $90°$ and that the fluoride ions are intercalated only into the CaO rock-salt layer. In addition, the positions of the oxygen vacancies in the figure are expressed based on an average. Further experimental and/or theoretical investigations are needed to clarify the detailed crystal structure of $Ca_2RuO_{2.5}F_2$.

Figure 6 compares the ρ values of the Ca_2RuO_4 and $Ca_2RuO_{2.5}F_2$ films as a function of temperature (T). The ρ-T curve of the Ca_2RuO_4 precursor revealed insulating behavior; by contrast, the strained Ca_2RuO_4 thin films exhibit metallic conduction [27], suggesting a substantial influence of lattice strain on the transport properties of Ca_2RuO_4. Thus, it is speculated that our strain-relaxed film has the poorly conductive RuO_2 planes with a bond angle of $<180°$. With fluorination, the ρ of the film increased. The ρ (300 K) value of the $Ca_2RuO_{2.5}F_2$ film was $8.6 \times 10^{-2}\,\Omega\,cm$, which is ~ 30 times higher than that of the Ca_2RuO_4 precursor, $2.9 \times 10^{-3}\,\Omega\,cm$. Since the ionic radius of Ru^{3+} in the $Ca_2RuO_{2.5}F_2$ film is larger than that of Ru^{4+} in the Ca_2RuO_4 precursor film, it is speculated that the Ru–O–Ru bonds bend more with the fluorination. Although the electrical conductivity of oxides containing Ru^{3+} has not been reported so far, Ru compounds with Ru^{3+}, such as $RuCl_3$, show an insulating behavior [32]. Therefore, the insulating properties of $Ca_2RuO_{2.5}F_2$ thin films might be largely related to the electronic states of Ru. Moreover, the ρ-T curve of the $Ca_2RuO_{2.5}F_2$ film was well fitted by $\rho \propto T^{-1/3}$ in the 22–300 K temperature range (inset

of Fig. 6), indicating that the electrical conduction of the $Ca_2RuO_{2.5}F_2$ film was dominated by the 2D variable range hopping mechanism. The two-dimensionality of the conduction pathway is consistent with the crystal structure (see Fig. 5).

IV. CONCLUSIONS

We fabricated $Ca_2RuO_{2.5}F_2$ epitaxial thin films by the PVDF-mediated topochemical fluorination of the Ca_2RuO_4 precursor and investigated their electronic properties. The obtained fluorinated thin films had the chemical composition $Ca_2RuO_{2.5}F_2$ with Ru^{3+}, as determined by EDS and XPS, in contrast to the fluorination of Sr_2RuO_4 to $Sr_2RuO_3F_2$ with Ru^{4+}. XRD and STEM revealed that $Ca_2RuO_{2.5}F_2$ had only one F^- site in the CaO rock-salt blocks, unlike $Sr_2RuO_3F_2$, which has two inequivalent F^- sites in the SrO layers; this is probably due to the larger lattice distortion in the Ca_2RuO_4 precursor. The $Ca_2RuO_{2.5}F_2$ film was insulating, with a ρ (300 K) of $8.6 \times 10^{-2}\ \Omega\,cm$, and the ρ-T curve was well described by a 2D variable range hopping model. These results demonstrate that local distortion can substantially affect the topochemical fluorination of ruthenates.

[1] M. V. Lobanov, A. M. Abakumov, A. V. Sidorova, M. G. Rozova, O. G. D'yachenko, E. V. Antipov, J. Hadermann, and G. Van Tendeloo, Solid State Sci. **4**, 19 (2002).

[2] J. Wang, Y. Shin, N. Gauquelin, Y. Yang, C. Lee, D. Jannis, J. Verbeeck, J. M. Rondinelli, and S. J. May, J. Phys. Condens. Matter **31**, 365602 (2019).

[3] T. Onozuka, A. Chikamatsu, T. Katayama, Y. Hirose, I. Harayama, D. Sekiba, E. Ikenaga, M. Minohara, H. Kumigashira, and T. Hasegawa, ACS Appl. Mater. Interfaces **9**, 10882 (2017).

[4] E. Sullivan and C. Greaves, Mater. Res. Bull. **47**, 2541 (2012).

[5] L. D. Aikens, R. K. Li, and C. Greaves, Chem. Commun. 2129 (2000).

[6] R. K. Li and C. Greaves, Phys. Rev. B **62**, 3811 (2000).

[7] F. D. Romero, P. A. Bingham, S. D. Forder, and M. A. Hayward, Inorg. Chem. **52**, 3388 (2013).

[8] R. V. Shpanchenko, M. G. Rozova, A. M. Abakumov, E. I. Ardashnikova, M. L. Kovba, S. N. Putilin, E. V. Antipov, O. I. Lebedev, and G. Van Tendeloo, Phys. C Supercond. **280**, 272 (1997).

[9] C. Greaves, J. L. Kissick, M. G. Francesconi, L. D. Aikens, and L. J. Gillie, J. Mater. Chem. **9**, 111 (1999).

[10] A. M. Alekseeva, A. M. Abakumov, M. G. Rozova, E. V. Antipov, and J. Hadermann, J. Solid State Chem. **177**, 731 (2004).

[11] F. J. Berry, X. Ren, R. Heap, P. Slater, and M. F. Thomas, Solid State Commun. **134**, 621 (2005).

[12] T. Katayama, A. Chikamatsu, Y. Hirose, R. Takagi, H. Kamisaka, T. Fukumura, and T. Hasegawa, J. Mater. Chem. C **2**, 5350 (2014).

[13] E. J. Moon, Y. Xie, E. D. Laird, D. J. Keavney, C. Y. Li, and S. J. May, J. Am. Chem. Soc. **136**, 2224 (2014).

[14] T. Katayama, A. Chikamatsu, Y. Hirose, T. Fukumura, and T. Hasegawa, J. Sol-Gel Sci. Technol. **73**, 527 (2015).

[15] A. Chikamatsu, K. Kawahara, T. Shiina, T. Onozuka, T. Katayama, and T. Hasegawa, ACS Omega **3**, 13141 (2018).

[16] J. Wang, Y. Shin, E. Arenholz, B. M. Lefler, J. M. Rondinelli, and S. J. May, Phys. Rev. Mater. **2**, 073407 (2018).

[17] Y. Kobayashi, M. Tian, M. Eguchi, and T. E. Mallouk, J. Am. Chem. Soc. **131**, 9849 (2009).

[18] P. R. Slater, J. Fluor. Chem. **117**, 43 (2002).

[19] K. Kawahara, A. Chikamatsu, T. Katayama, T. Onozuka, D. Ogawa, K. Morikawa, E. Ikenaga, Y. Hirose, I. Harayama, D. Sekiba, T. Fukumura, and T. Hasegawa, CrystEngComm **19**, 313 (2017).

[20] T. Maruyama, A. Chikamatsu, T. Katayama, K. Kuramochi, H. Ogino, M. Kitamura, K. Horiba, H. Kumigashira, and T. Hasegawa, J. Mater. Chem. C **8**, 8268 (2020).

[21] A. Chikamatsu, Y. Kurauchi, K. Kawahara, T. Onozuka, M. Minohara, H. Kumigashira, E. Ikenaga, and T. Hasegawa, Phys. Rev. B **97**, 235101 (2018).

[22] C. S. Alexander, G. Cao, V. Dobrosavljevic, S. Mc Call, J. E. Crow, E. Lochner, and R. P. Guertin, Phys. Rev. B **60**, R8422 (1999).

[23] S. J. Moon, M. W. Kim, K. W. Kim, Y. S. Lee, J.-Y. Kim, J.-H. Park, B. J. Kim, S.-J. Oh, S. Nakatsuji, Y. Maeno, I. Nagai, S. I. Ikeda, G. Cao, and T. W. Noh, Phys. Rev. B **74**, 113104 (2006).

[24] E. Gorelov, M. Karolak, T. O. Wehling, F. Lechermann, A. I. Lichtenstein, and E. Pavarini, Phys. Rev. Lett. **104**, 226401 (2010).

[25] K. Momma and F. Izumi, J. Appl. Crystallogr. **44**, 1272 (2011).

[26] See Supplemental Material at http://link.aps.org/supplemental/10.1103/PhysRevMaterials.6.035002 for 2D 2θ-χ images, magnified lattice images of the films, obtained via cross-sectional ADF-STEM, and schematic crystal structures of $Ca_2RuO_{2.5}F_2$ along [100].

[27] C. Dietl, S. K. Sinha, G. Christiani, Y. Khaydukov, T. Keller, D. Putzky, S. Ibrahimkutty, P. Wochner, G. Logvenov, P. A. van Aken, B. J. Kim, and B. Keimer, Appl. Phys. Lett. **112**, 031902 (2018).

[28] P. R. Slater and R. K. B. Gover, J. Mater. Chem. **12**, 291 (2002).

[29] D. Drouin, A. R. Couture, D. Joly, X. Tastet, V. Aimez, and R. Gauvin, Scanning **29**, 92 (2007).

[30] T. Katayama, A. Chikamatsu, K. Yamada, K. Shigematsu, T. Onozuka, M. Minohara, H. Kumigashira, E. Ikenaga, and T. Hasegawa, J. Appl. Phys. **120**, 085305 (2016).

[31] H. Lu, Y. Yang, Z. Luo, S. Wu, Y. Ji, Y. Li, J. Zhang, G. Liu, Y. Jiang, H. Yang, C. Ma, R. Zhao, and J. Gao, Mater. Res. Express **7**, 126402 (2020).

[32] L. Wang, M. Rocci-Lane, P. Brazis, C. R. Kannewurf, Y.-I. Kim, W. Lee, J.-H. Choy, and M. G. Kanatzidis, J. Am. Chem. Soc. **122**, 6629 (2000).